Flow Past a Sphere: Topological Transitions of the Vorticity Field

Susumu Shirayama*
Institute of Computational Fluid Dynamics, Tokyo 152, Japan

On the basis of unsteady three-dimensional structures in a separated flowfield and of the visualization techniques for unsteady phenomena, the flowfield of a sphere placed in a uniform flow is analyzed numerically. In the initial flowfield, an axisymmetric flow structure characterizes this field. A topological transition suddenly takes place, and a periodical structure appears in the wake region. These structures are visualized and confirmed by analyzing the vector fields (velocity and vorticity fields). In these unsteady flowfields, the initial flowfield is defined by an axisymmetric structure but the developed field does not have the axisymmetry. A plane-symmetry, however, appears and is preserved.

Introduction

ON the assumption that the wake has a periodical structure and that a quasi-steady-state solution indicates an average flowfield, the practical computations to investigate the aerodynamic features have been performed. In the computations of steady-state flowfields, an influence of the far wake on the boundary layer is predicted to be negligible because of this assumption. In other words, the body forces, the separation line, and other aerodynamic features on the body surface are determined only by the near wake structure. On the other hand, numerous recent investigations of computational fluid dynamics for aerodynamics have tried to verify this assumption and shed light on the characteristic features of unsteady flowfields.[1] In spite of these efforts, however, few unsteady wake structures and separation patterns around a bluff body have been confirmed, especially in three-dimensional flowfields.[1-3]

In this paper, we investigate the topological changes of an axisymmetric vorticity field on behalf of the typical vortical structure in the unsteady flowfields. To obtain a basic structure of such a flowfield, we treat the moderate Reynolds-number flow around a sphere.

Numerical Approach

The flowfields are obtained by solving the incompressible Navier-Stokes equations. Instead of solving the continuity equation, the pressure equation is introduced by using the Helmholtz decomposition of the Navier-Stokes equations.[4] Therefore, in the present method, the pressure equation and the Navier-Stokes equations are solved. All equations mentioned above are written in generalized curvilinear coordinates and are solved by a finite difference method. First, general curvilinear coordinates are introduced[5]:

$$a^i = \nabla \xi^i, \qquad g^{ij} = a^i \cdot a^j, \qquad (U)_i = a^i \cdot u$$

$$(i, j = 1, 2, 3) \tag{1}$$

where a^i is the contravariant base-vector, g^{ij} is the contravariant metric tensor, U is the contravariant velocity vector, and

$(.)_i$ is the component in the i-direction. By using these relations, the pressure equation and the Navier-Stokes equations are transformed as follows:

$$g^{ij} p_{\xi^i \xi^j} + a^i [a^j]_{\xi^i} p_{\xi^j}$$

$$= (\delta_{ij} - 2) \cdot ((a^i)_i [u^i]_{\xi^i})((a^j)_i [u^j]_{\xi^j}) + \frac{(a^i u_{\xi^i})_h}{\Delta t} \tag{2}$$

$$\frac{\partial u^l}{\partial t} + U^i u^l_{\xi^i} = -a^i p_{\xi^i} + \frac{1}{Re}(g^{ij} u^l_{\xi^i \xi^j} + a^i [a^j]_{\xi^i} u^l_{\xi^j})$$

$$(i, j, l = 1, 2, 3) \tag{3}$$

where the subscript ξ^i on the bracket indicates partial differentiation and $(.)_h$ denotes an approximation to a partial differential operator. The Euler implicit scheme (first or second order) is used for the time integration. All spatial derivatives except the nonlinear terms are approximated by central differences. The nonlinear terms are approximated by the following third-order upwind scheme[2,6]:

$$\left(U \frac{\partial u}{\partial \xi}\right)_i = U_i \frac{-u_{i+2} + 8(u_{i+1} - u_{i-1}) + u_{i-2}}{12\Delta \xi}$$

$$+ \alpha \cdot |U_i| \frac{u_{i+2} - 4u_{i+1} + 6u_i - 4u_{i-1} + u_{i-2}}{12\Delta \xi} \tag{4}$$

where α takes 1 or 3.

We use the Lagrangian approach in our flow visualization. In this approach, the separation patterns on the body surface and the wake structure are identified by tracing particle paths or vortex lines. These points and lines are determined by solving the following autonomous or nonautonomous dynamic system:

$$\frac{dx}{ds} = b \tag{5}$$

where x defines a space in which the solution moves, and b is considered as the velocity vector or the vorticity vector. In the case of an autonomous system, b is the function of the variables x, and s is the distance along the streamlines or the vortex lines. In the case of a nonautonomous system, s denotes the time increment. The vector b is the function of the variables x and s. We solve Eq. (5) directly or examine the critical point. For further detail about these techniques, see Refs. 3 and 7. A brief statement about the accuracy of numerical

integration of Eq. (5) is in Appendix A, and the critical-point concept is discussed in Appendix B.

Results

The grid system and its topology are shown in Fig. 1a. As demonstrated in Figs. 1b and 1c, we use the C-type or O-type grid system in a sectional plane. That is, the O-C type or O-O type grid system is utilized in this computation. To validate the present approach, one first checks cases with low Reynolds numbers. The number of grid points is $34 \times 80 \times 34$ or $50 \times 100 \times 50$ with the O-C type grid system. Fig. 1b shows the case of $50 \times 100 \times 50$ grid points. The flowfields are characterized by a single vortex ring behind the body and reach
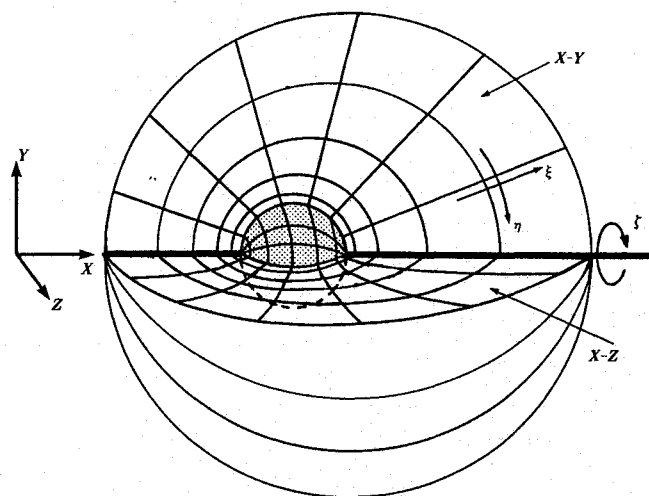

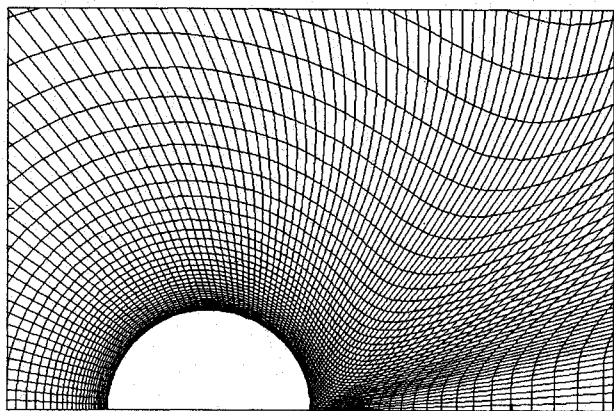Fig. 1a Schema of a grid system and its topology.

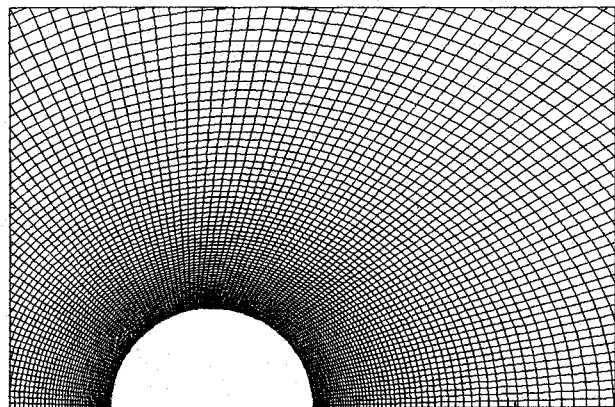Fig. 1b Longitudinal cross section of the three-dimensional O-C type grid.

Fig. 1c Longitudinal cross section of the three-dimensional O-O type grid.

the steady state. These solutions are mesh-converged in the flowfields at Reynolds numbers between 10 and 150. The Reynolds number is based on the diameter. The results in Tables 1 and 2 and Fig. 2 are obtained by using the O-C type grid system with $50 \times 100 \times 50$ grid points. The relation between the drag coefficient and the Reynolds number is shown in Table 1. Present results agree well with other results.[8-12] Figure 2 demonstrates variation of the eddy length and the separation angle with the Reynolds number. These are compared with other results.[8,9,13,14] Our results are also shown in Table 2. Present results are in fair agreement with other results. In our computation, a vortex ring appeared in the case of $Re = 20$, whereas we cannot observe the separation in the case of $Re = 10$. It is the first topological transition of the vorticity field. Concerning the critical Reynolds number (Re_c) at which a permanent vortex ring begins to form, we extrapolate in Fig. 2 and acquire $Re_c = 19$. Previous results[8-14] were obtained by using numerical methods, except Taneda's experimental work.[13] Numerical methods utilized in previous work are aimed at solving the governing equations for the vorticity and axially symmetric stream function and are classified into the relaxation methods,[8,10,14] the time-dependent methods,[9] and the semianalytical methods.[11,12]

Since a numerical instability caused by the skewness of the O-C type grid system (near the rear stagnation point) affects the unsteady flow pattern, the O-O type grid system is utilized to investigate the unsteady separated structure. The number of grid points is $50 \times 50 \times 81$ or $200 \times 100 \times 81$. Fig. 1c demonstrates the case of $200 \times 100 \times 81$ grid points. The Reynolds number is 500. The simulation time is nondimensionalized by the diameter and the speed of the body. The results with the fine grid system are presented most often.

First, we explain the global feature of this flowfield by using a pressure distribution. The body is at rest initially and then is accelerated until the speed reaches unity. It takes five dimensionless time units to accelerate the body. In the initial stage, a vortex ring characterizes this axisymmetric flowfield. The vortex ring develops as time goes on, and the flowfield reaches equilibrium once. The pressure distributions at $t = 22.5$ are shown in Fig. 3. The drag coefficient is 0.503 in this stage. Surface streamlines on the body in a rear view and the patterns of grid-surface streamlines on the x-z plane are shown in Fig. 4. The eddy length is 1.63, and the separation angle is 75.3 deg. The region indicated by S_2 in Fig. 4 is not a reversed flowfield at this Reynolds number but will be separated if the Reynolds number becomes larger. As discussed in Anderson et al.,[15] the solution of the Navier-Stokes equations with symmetric initial conditions should remain symmetric as a flow evolves. From this, it may be concluded that the flowfield in the above computation reaches to the steady state. However, according to experiments,[16-19] if the Reynolds number exceeds about 250 unsteady flow with a nonaxisymmetrical structure occurs. We continue the computation from $t = 22.5$ and find a nonaxisymmetrical flow pattern at $t = 30.0$. Figure 5 shows the time variation of equipressure surface. (We plot two levels of pressure: $C_p = -0.44$ and -0.4.) This is the second topological transition. Since we have not introduced perturbations, such asymmetry is caused by numerical errors. If we use the expression of Ref. 15, it can be said that the axisymmetric flowfield in this range of the Reynolds number is unstable, and instability occurs for the unexpected numerical errors after a significant length of time (about 30 in this computation). Although a fixed perturbation plays an important role in computing the vortex-shedding flowfields, as pointed out in Ref. 15, it is difficult to investigate what kinds of perturbations cause the instability in the flow past a sphere. This is because the structure of an unsteady flowfield has not been established during the past two decades.[3,16-19] Recently, the linear stability of the steady axisymmetric base flow was reported by Kim and Pearlstein.[20] They showed that the axisymmetric base flow undergoes a Hopf bifurcation at $Re =$

Table 1   Comparison of the drag coefficient with the other results

Re	Drag coefficient					
	Present	Jenson[8]	Rimon[9]	Le Clair[10]	Dennis[11]	Nakabayashi[12]
10	4.255	4.840	4.410	4.288	4.424	4.298
20	2.622	2.946	———	2.711	2.730	2.707
30	2.066	———	———	2.110	———	2.104
40	1.741	1.860	1.860	———	1.808	1.771
50	1.532	———	———	———	———	1.555
60	1.427	———	———	———	———	1.402
70	1.313	———	———	———	———	1.285
80	1.222	———	———	———	———	1.194
90	1.149	———	———	———	———	1.119
100	1.104	———	———	1.096	———	1.057
150	0.901	———	———	———	———	———
200	0.784	———	———	0.772	———	———

Table 2   Variations of the eddy length and the separation angle with the Reynolds number

Re	L/D	θ (deg)
10	———	———
20	0.029	5.9
30	0.145	25.7
40	0.289	32.5
50	0.386	39.6
60	0.502	43.5
70	0.592	45.9
80	0.675	48.2
90	0.772	51.2
100	0.844	52.8
150	1.141	59.1
200	1.310	62.0

175.1, with the critical disturbance having an azimuthal wavenumber $m = 1$ and a Strouhal number 0.0955. From Fig. 5, we find a result similar to their analysis. The vortex ring inclines, and the center of the core of the vortex ring exists in a certain inclined plane. A plane of symmetry in the flowfield appears near the x-y plane. Also, the higher frequent disturbance cannot be observed. This corresponds to the result of Kim and Pearlstein. It is considered that the instability is caused by the disturbance having azimuthal wavenumber $m = 1$. By continuing the computation, the time-development pressure distributions on the x-y plane and the x-z plane are obtained in Fig. 6. In these figures, the developed flowfields are presented, and the periodicity of the flowfield is observed in the pressure fields. We can observe a vortex street like the Kármán vortex in Fig. 6a. The developed flow pattern is not axisymmetric, but the symmetric plane is preserved. This symmetric plane nearly coincides with the x-y plane in the case of this practice. Since we have not introduced the fixed perturbations, a location of this plane cannot be predicted. However, if the location is determined, the position is stable for time variation of the flowfield in this range of the Reynolds number. Here we show the quantitative comparison with experiments and the feature of this periodicity. A time history of the force coefficients is presented in Fig. 7a. The average drag coefficient is 0.554. This value is plotted with the values of cases of low Reynolds numbers in Fig. 7b. The solid line in Fig. 7b is reproduced from Schlichting.[21] Two modes are observed in the variation of the force coefficient in the y-direction. The Strouhal numbers of these modes are 0.204 and 0.125. In experiments,[16,19] the Strouhal number is about 0.2 at Reynolds number 500.

Next we show the topological transitions from the standpoint of time variation of the boundary layers. Time development of the patterns of surface streamlines on the body in the rear view is shown in Figs. 4a and 8. It is also shown that the axisymmetry has been broken down, and the plane of symmetry in the flowfield appears near the x-y plane. The
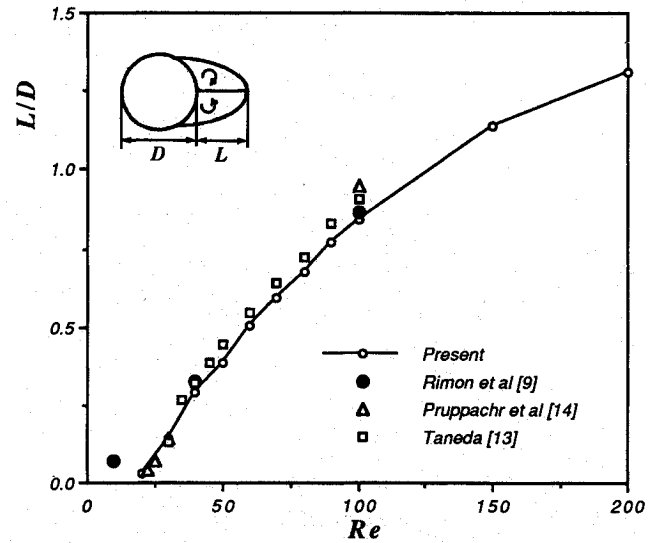

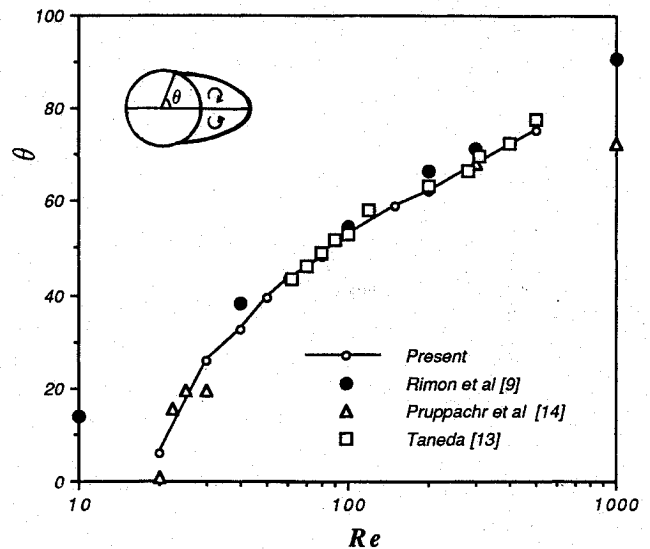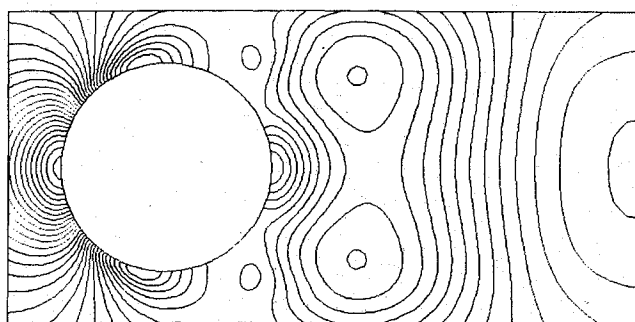Fig. 2a   Comparison of the variation of the eddy length with the other results.
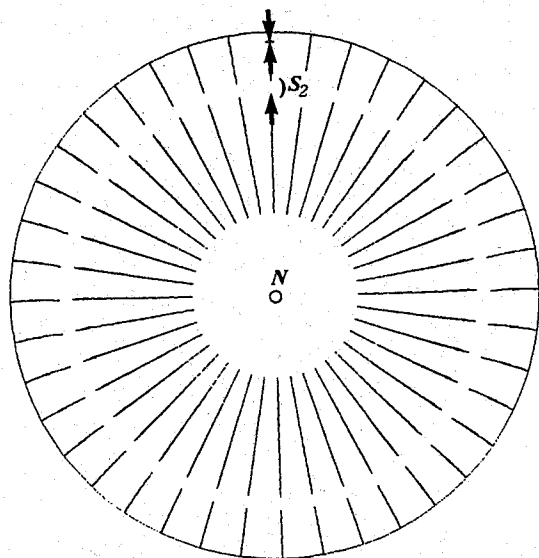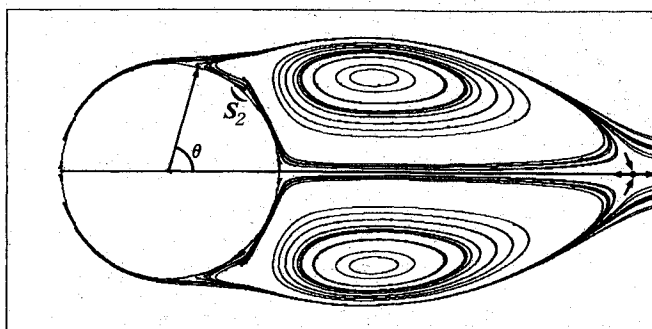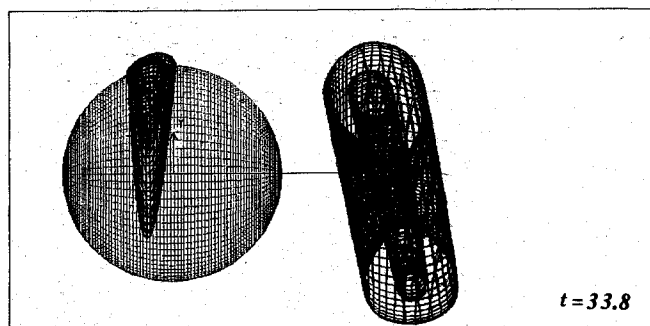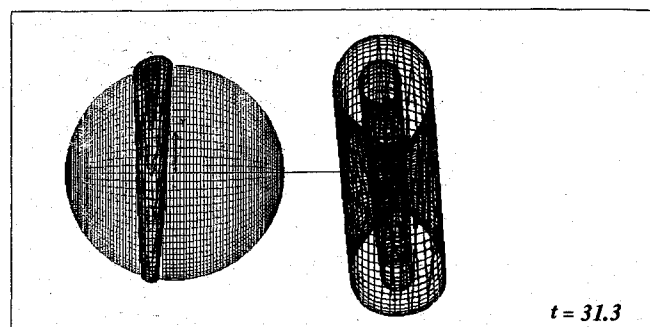

Fig. 2b   Comparison of the variation of the separation angle with the other results.

sequence of the topological changes is observed on the body surface. The critical points are classified according to Appendix B. The characters S_a, N, and F denote a saddle, a node, and a focus, respectively. Initially, topological structure is characterized by the front and rear stagnation points, and these stagnation points are defined as the star-nodes. As time

Fig. 3   Pressure distributions on the x-y plane at t = 22.5.

Fig. 4a   Pattern of surface streamlines on the body at t = 22.5 (in rear view).

Fig. 4b   Pattern of surface streamlines on the x-y plane at t = 22.5.

Fig. 5   Time variation of equipressure surfaces: C_p = −0.44 and −0.4.

move on the separation line. It is expected that this structure is related to the periodical structure that appeared in the wake region. In these figures, we emphasize that, in all stages, the following topological rule[22] about critical points on the body surface is satisfied:

$$\sum_{N,F} - \sum_{S_a} = 2$$

The final objective of our research is to study the relation between these separation patterns and the pattern of the wake structure. Therefore, we try to visualize the flowfield in the wake region. First, the frozen field at t = 41.3 is investigated. As shown in Fig. 9, the initial vortex ring has become inclined and deformed. At this time, the next vortex has appeared in the lower part of the sphere. It seems that the initial and the next vortices cause many critical points (in Fig. 8c). In such critical points, the focus interests us because it seems that the vortices start from this critical point in the boundary layer. The instantaneous streamlines are shown in Fig. 10. Those streamlines having initial positions in the neighborhood of the foci are rolled up and pulled into the deformed initial vortex ring. After the initial vortex ring flows out from the near wake, the equilibrium flowfields appear. Figure 11 shows the particle traces corresponding to the integrated streaksheet in the experiment. The particles are generated on several points near the body surface at every five time steps. The qualitative feature indicated by these figures is in accord with several experiments.[16-19] The periodical structure with the symmetrical plane is clearly observed (in Figs. 11a and 11b). The visualization in Fig. 11 is a very efficient way to obtain qualitative information and to verify the reliability of the unsteady solution by comparing it with the experiment. According to our previous work, however, the instantaneous flowfields (the frozen flowfields) do not coincide with this integrated streaksheet in general description.[3] Therefore, several visualizations are performed in the frozen field. In Fig. 12a, the differences between the pattern of instantaneous streamlines and the integrated streaksheet shown in Fig. 11a can be found. In the near wake region, the differences are slight but the portion of clustering particles (indicated by character C in Fig. 12a)
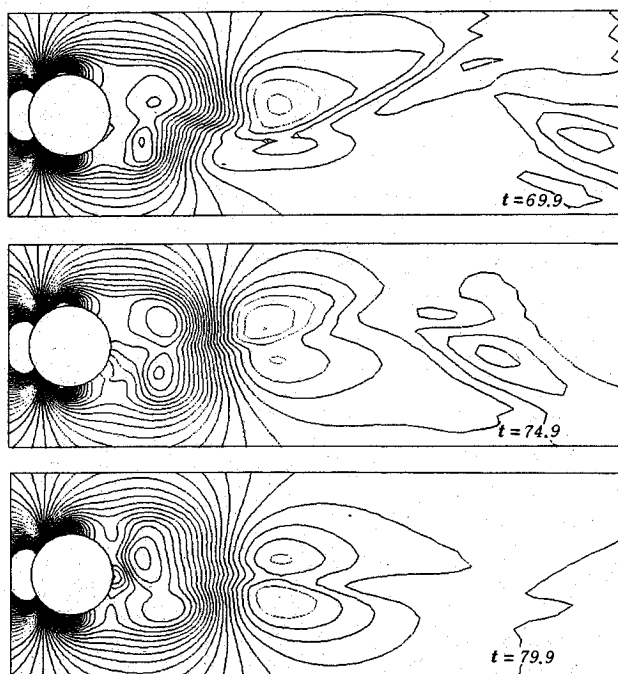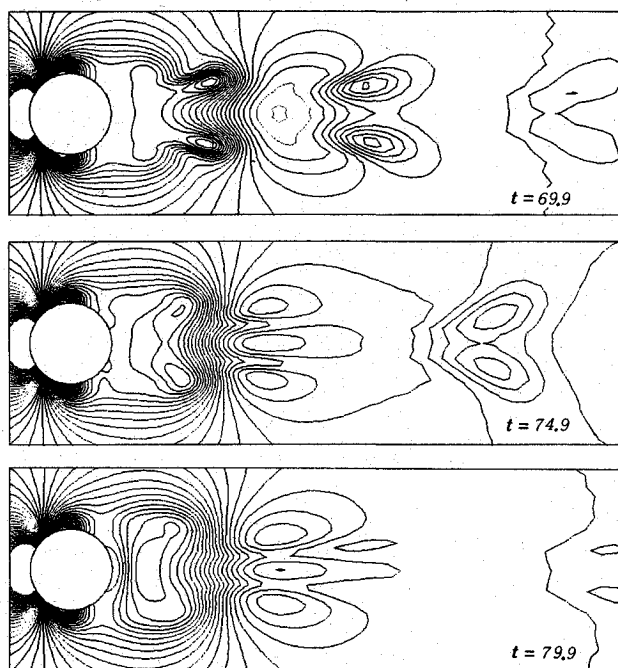
goes on, the boundary layer separates, but the axisymmetrical structure is preserved (Fig. 4a). The rear stagnation point changes from the stable star-node to the unstable star-node. The points on the separation line are node-saddles. Suddenly, the axisymmetry is broken, and then innumerable node-saddles change to one saddle point and one nodal point on two locations where the separation line and the symmetry plane cross each other, as seen in Fig. 8a. In Fig. 8b, a new pair of saddle and nodal points appears. This saddle point exists in the portion indicated by S_2 in Fig. 4a. Then the nodal point changes to the saddle and the foci, as shown in Fig. 8c. Also, other saddle points and nodal points are observed in the lower part of Fig. 8c and on the separation line. Most critical points disappear after the initial vortex ring flows out from near wake in Fig. 8d. In the developed stage, we cannot find the critical points except the rear stagnation point in the separated flow region (see Figs. 8e and 8g). In this stage, two saddle points

Fig. 6a Time-development pressure distributions on the x-y plane.

Fig. 7a Time history of force coefficients.

Fig. 6b Time-development pressure distributions on the x-z plane.

Fig. 7b Relation between the drag coefficient and the Reynolds number. Solid line is reproduced from Schlichting.[21]

are not observed in the streamline pattern. As shown in Fig. 12b, the weak vorticity exists in that region (the density of vortex lines is scarce). The vortex lines show the longitudinal vortical structure and the periodic pattern in the wake. Any vortex line consists of a certain vortex loop. (Arrows in Fig. 12b indicate the direction of vortex lines.) From the integrated streaksheet (Fig. 11) and the instantaneous flowfield (Fig. 12), it is found that the fluid particles that exist in portion C were parts of the vortex rings in the near wake, have become parts of the longitudinal vortex, and flow out to the far wake periodically. The vortical structure in the wake is represented by nearly axisymmetric vortex loops in the near wake and longitudinal vortex loops. In this way, an unsteady flowfield
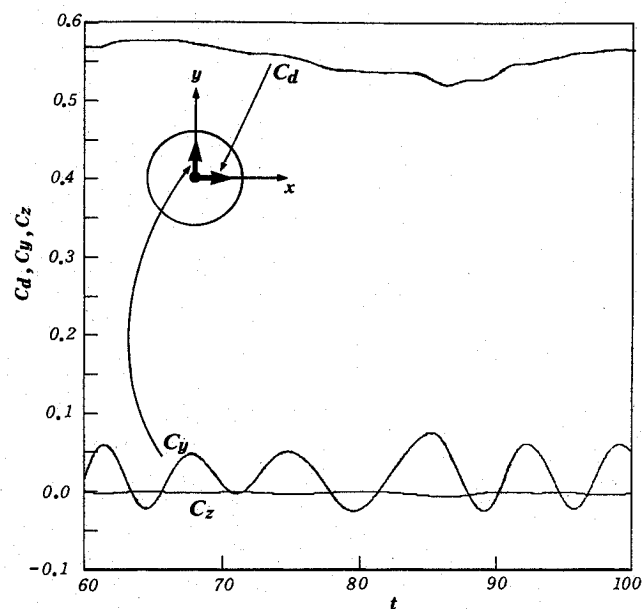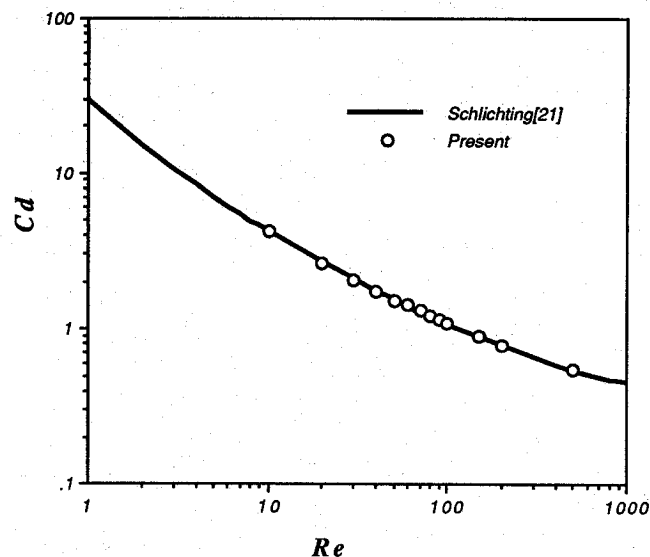
around a sphere has been observed, and several global features of the flow have been obtained by the present computations. However, further detailed investigations are required for several unsolved problems: a fixed perturbation, a position of a plane symmetry, the Strouhal number bifurcation, etc.

Finally, we compute the same flowfields by using the coarse grid system. The average drag coefficient is 0.538 in this case. This value is a little bit smaller than in the case of the fine grid system. The Strouhal number is 0.133, and the long periodic motion is recognized only from the time history of the force coefficients. The differences of the drag coefficient and the smaller Strouhal number between the coarse grid and the fine grid are very small. The large Strouhal number (about 0.2), which corresponds to experimental results, is not obtained on the coarser grid system. Although the longitudinal vortices are observed in coarser grid cases, the strength of the vortices is very weak, and the longitudinal structure is not clearly captured. It may be that the large Strouhal number is caused by the behavior of the longitudinal vortices. We may require more grid points to resolve this mechanism.
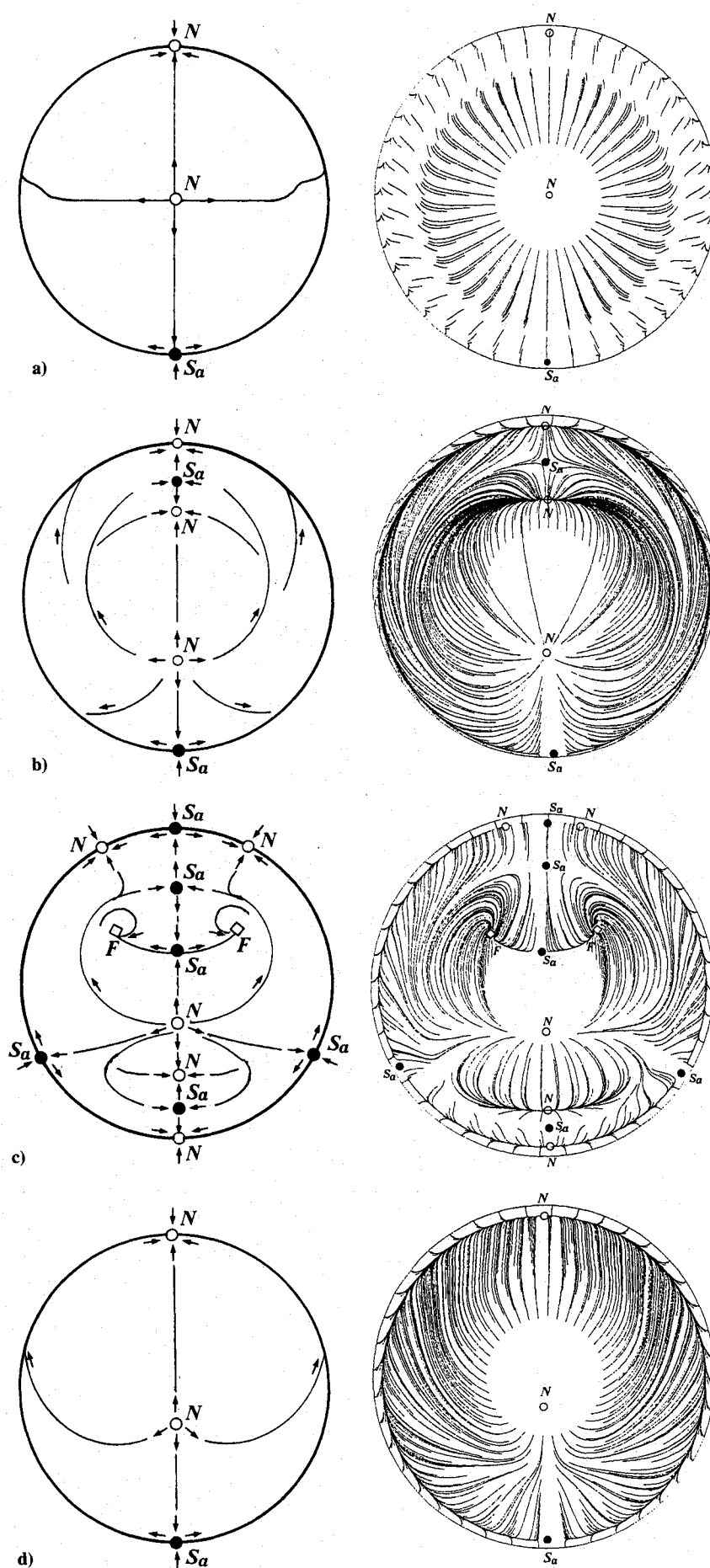
Fig. 8   Time evolution of the patterns of surface streamlines on the body surface and its topological representations: a) $t = 30.0$; b) $t = 37.5$; c) $t = 41.3$; d) $t = 45.0$.
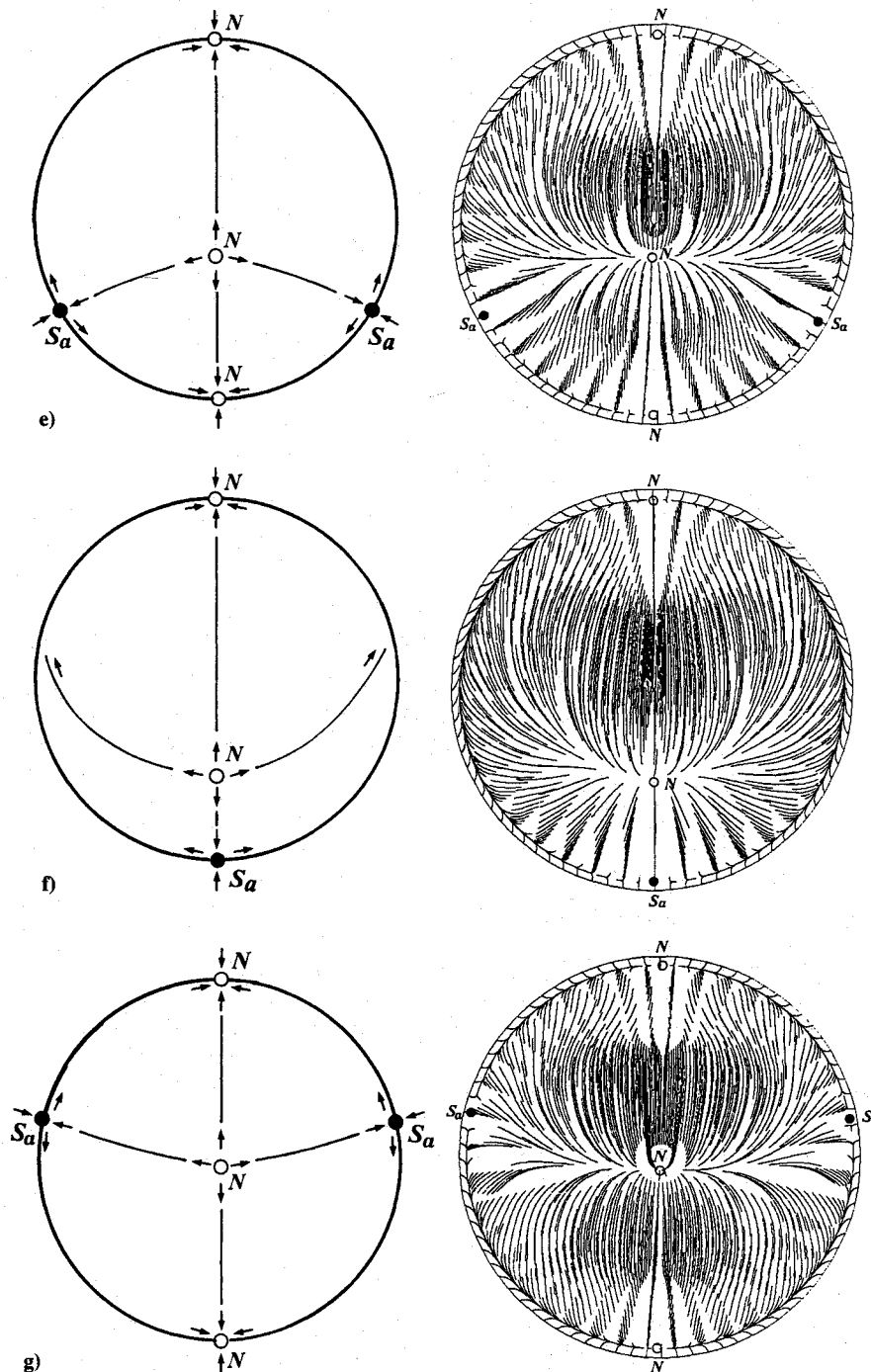
Fig. 8 (continued) Time evolution of the patterns of surface streamlines on the body surface and its topological representations: e) t = 72.4; f) t = 74.9; g) t = 79.9.

Conclusions

On the basis of unsteady three-dimensional structures in a separated flowfield and the visualization techniques for unsteady phenomena, the flowfield of a sphere placed in a uniform flow has been analyzed numerically. We observed the primary separation at Reynolds number 20. The estimated critical Reynolds number is 19 in our computations. The flowfields are characterized by an axisymmetric flow structure (one vortex ring) at low and intermediate Reynolds numbers. The global features of these flowfields are defined by the drag coefficient, the variation of eddy length, and the separation angle with the Reynolds number. Present results are in good agreement with other results.

If the Reynolds number is raised to 500, unsteady flow patterns appear. In the initial flowfield, an axisymmetric flow structure characterizes this field. As time evolves, a nonaxisymmetric flow pattern appears. This pattern is the same as that predicted by the linear stability analysis. A sequence of the topological transitions takes place, and a periodical structure appears in the wake region. The drag coefficient is in good agreement with several experiments, even when a coarse grid system is utilized in the computations. A streamwise vortical structure can be clearly observed by using the fine grid system with the far wake region. This may be recognized as the secondary structure in the wake region and slightly affects the states of the boundary layer. Concerning the Strouhal number, the fine grid computation gives two values. The
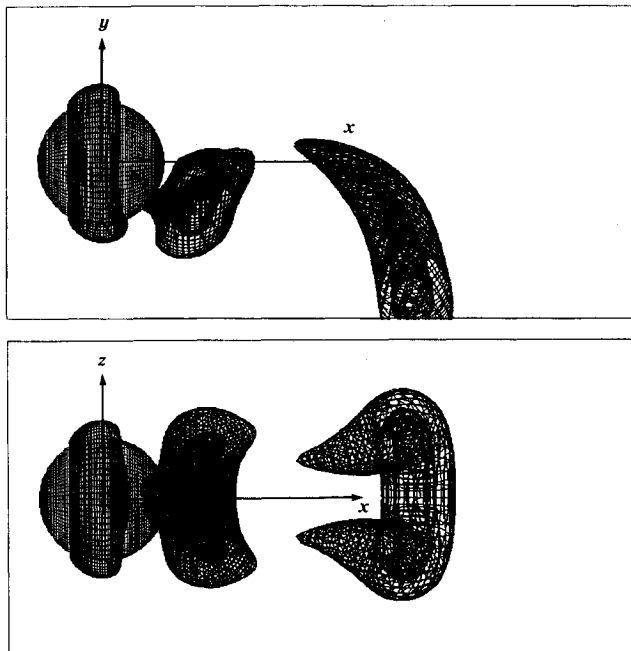
Fig. 9   Equipressure surfaces at $t = 41.3$ ($C_p = -0.6$ and -0.3).

evolution of the secondary structure may be related to this Strouhal number bifurcation and may play an important role in predicting the time-dependent behavior of the wake. However, further investigations are required to explain the mechanism of this bifurcation.

Appendix A: Numerical Integration Methods

Several authors have discussed the accuracy of trajectory integration.[23,24] We also investigate this subject by using the model velocity field proposed in Ref. 23. The model set of equations is

$$\begin{pmatrix} b^1 \\ b^2 \end{pmatrix} = \frac{d}{ds} \begin{pmatrix} x_1 \\ x_2 \end{pmatrix} = \begin{pmatrix} \alpha & -\beta \\ \beta & \alpha \end{pmatrix} \begin{pmatrix} x_1 \\ x_2 \end{pmatrix} \quad (A1)$$

For convenience, we consider that two parameters (α, β) are represented by using one parameter θ as follows: $\alpha = \cos\theta$ and $\beta = \sin\theta$. Here $x(s + \delta s)$ is approximated by expanding around s up through the second order:

$$x(s + \delta s) = x + \frac{dx}{ds} \cdot \delta s + \frac{1}{2} \cdot \frac{d^2x}{ds^2} \cdot \delta s^2 \quad (A2)$$

Substituting for dx/ds and d^2x/ds^2 in Eq. (A2) from Eq. (A1), Eq. (A2) is represented by

$$x(s + \delta s) = x + C \cdot x \cdot \delta s + \tfrac{1}{2} \cdot D \cdot x \cdot \delta s^2 \quad (A3)$$

where

$$C = \begin{pmatrix} \cos\theta & -\sin\theta \\ \sin\theta & \cos\theta \end{pmatrix} \text{ and } D = \begin{pmatrix} \cos2\theta & -\sin2\theta \\ \sin2\theta & \cos2\theta \end{pmatrix}$$

If s is taken as time t, $C \cdot x$ means the velocity and $D \cdot x$ means the acceleration.

Then we consider the geometrical interpretation of matrices C and D. From the second term in the right side of Eq. (A3), matrix C rotates the vector x with angle θ. Also, matrix D rotates the vector x with angle 2θ. Fig. 13 shows the geometrical interpretation of the operators C and D in the case that θ takes a value between 0 deg and 180 deg. If a first-order-accurate method is used for the integration, the following remarks are derived from these considerations:

1) If 0 deg $< \theta <$ 180 deg the numerical trajectory always detaches from the exact trajectory to the outward direction of the origin.

2) If 180 deg $< \theta <$ 360 deg, the numerical trajectory always detaches from the exact trajectory to the inward direction of the origin.

In this way, if the step size δs is not small, it is found that the first-order-accurate method is not desired for the trajectory integration. Therefore, in our computation, a second-order-accurate predictor-corrector method has been utilized.
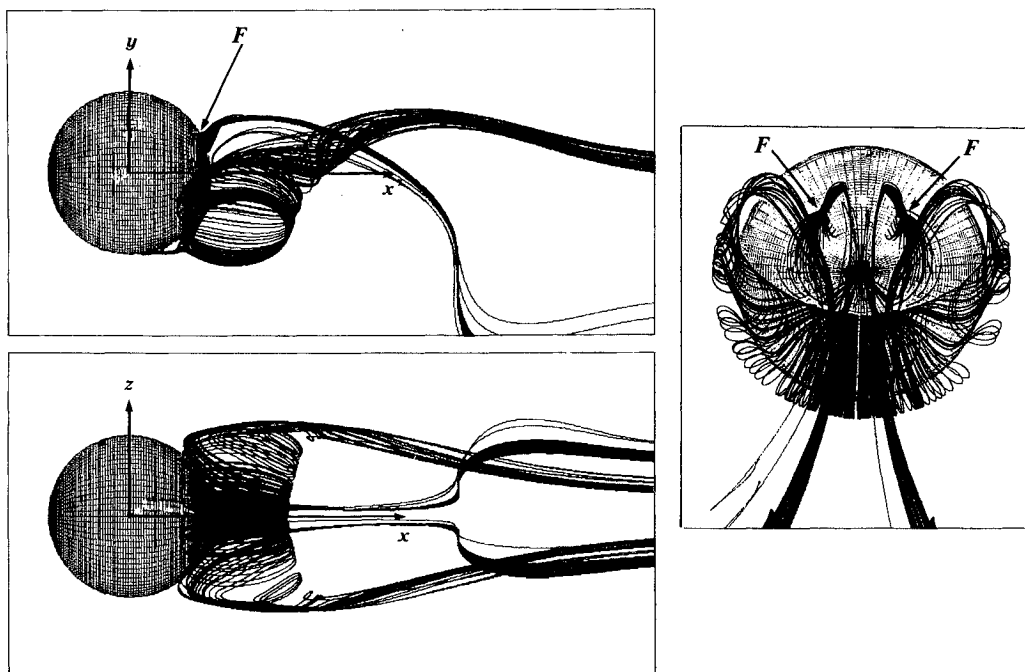

Fig. 10   Instantaneous streamlines at $t = 41.3$. View from the z-direction (top left), the x-direction (right), and the y-direction (bottom left).
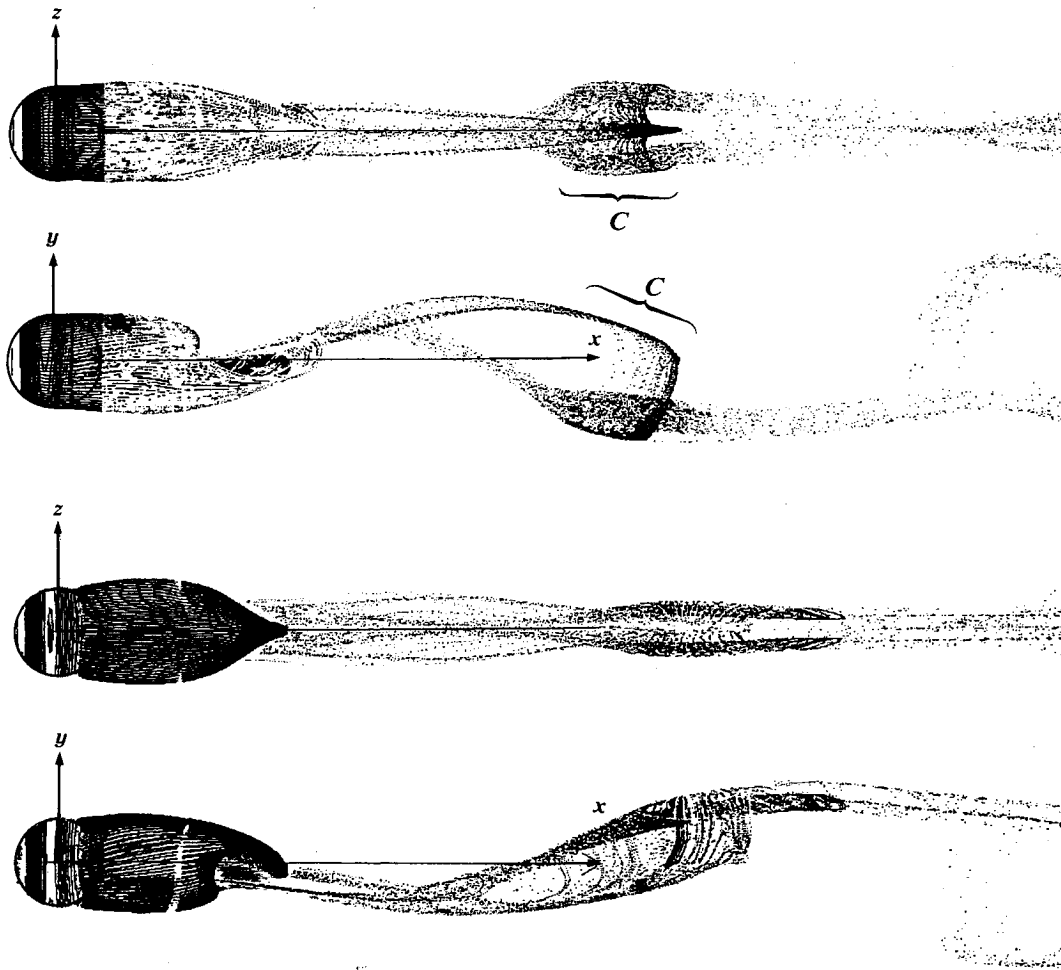
Fig. 11 Computed particle traces and pressure contours on the body surface. View from the z-direction (top) and the y-direction (bottom). a) t = 74.9; b) t = 78.6.

Appendix B: Critical-Point Concepts

The global characteristic feature of the solution will be examined by the linearization of Eq. (5) around a critical point. The critical points are defined as follows:

$$\frac{b^i}{b^j} = \frac{0}{0} \quad \text{for} \quad i \pm j \tag{B1}$$

The classification of the critical point indicates the global characteristic of the solution. To classify the critical point, one expands Eq. (5) and linearizes it around a certain point C. The linearized equation is as follows:

$$\frac{dx}{ds} = E \cdot x + b_c \tag{B2}$$

where $E_{ij} = \partial b^i/\partial x^j$. If point C is a critical point, the classification of the critical point is performed by inquiring into the eigenvalues and the eigenvectors of matrix E. Since E is the 3 x 3 real matrix, one eigenvalue is always real. We have to
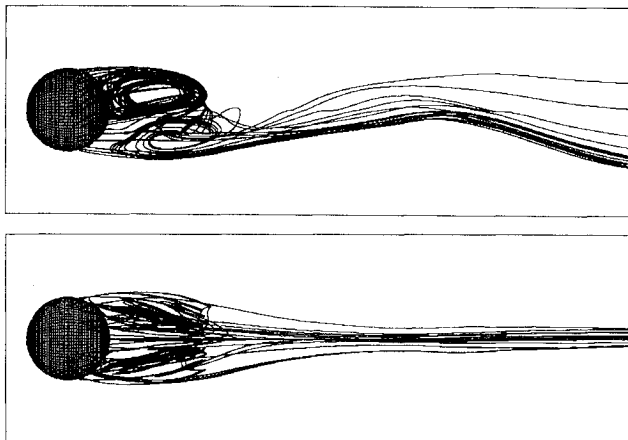

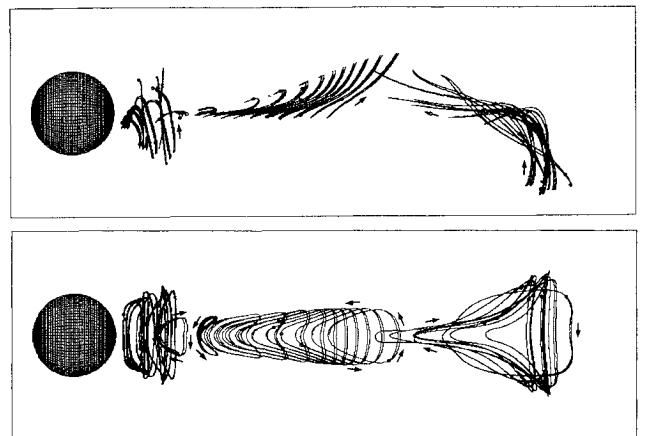Fig. 12a Instantaneous streamlines at t = 74.9. View from the y-direction (top) and the z-direction (bottom).

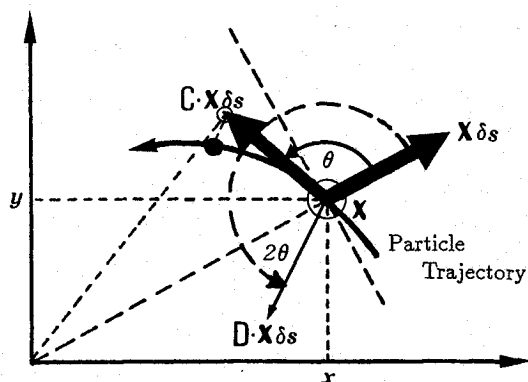Fig. 12b Instantaneous vortex lines at t = 74.9. View from the y-direction (top) and the z-direction (bottom).

Fig. 13 Geometrical interpretation of matrices *C* and *D*.

classify the vector field around the critical points for the four cases based on the eigenvalues: three different real eigenvalues, one and double real eigenvalues, triple real eigenvalues, and one real and conjugate complex eigenvalues. In each case, there is at least one plane that contains solution trajectories. This plane is obtained by a certain coordinate transformation $y = Px$. According to Perry and Chong,[25] we examine the following two-dimensional equations on such a plane instead of investigating the three-dimensional system.

$$\frac{d}{ds}\begin{pmatrix} y_1 \\ y_2 \end{pmatrix} = \begin{pmatrix} a & b \\ c & d \end{pmatrix}\begin{pmatrix} y_1 \\ y_2 \end{pmatrix} \qquad (B3)$$

Note that similar equations are derived directly in the case of the classification of the surface streamlines.[22] Then we classify the critical points according to the eigenvalues of Eq. (B3). The eigenvalues are $\lambda_1 = -(p/2) - (\sqrt{p^2 - 4q})/2$ and $\lambda_2 = -(p/2) + (\sqrt{p^2 - 4q})/2$, where $p = -(a + d)$ and $q = ad - bc$.

1) In the cases where the eigenvalues are real:
   1.1) $\lambda_1 < \lambda_2 < 0$, then the critical point is named a stable node.
   1.2) $0 < \lambda_1 < \lambda_2$, an unstable node.
   1.3) $\lambda_1 < 0 < \lambda_2$, a saddle point.
   1.4) $\lambda_1 = \lambda_2 < 0$, a stable star node.
   1.5) $0 < \lambda_1 = \lambda_2$, an unstable star node.
   1.6) $\lambda_1 = 0$ or $\lambda_2 = 0$, a node-saddle point.
2) In the cases where the eigenvalues are complex:
   2.1) $-(p/2) < 0$, a stable focus.
   2.2) $-(p/2) > 0$, an unstable focus.
   2.3) $-(p/2) = 0$, a center or a circle.

The model equation in Appendix A is the case that eigenvalues are the conjugate complex in two dimensions. If $\alpha > 0$, the solution has the unstable focus. If $\alpha < 0$, the solution is characterized by the stable focus. In the case of $\alpha = 0$, the solution is represented by a circle. Concerning direct approaches for the three-dimensional system, see Refs. 25 and 26.

References

[1]Grinstein, F. F., Boris, J. P., Griffin, O. M., Hussain, F., and Oran, E. S., "Three-Dimensional Coherent Structure Dynamics in Spatially Evolving Bluff-Body Wake Flows," AIAA Paper 90-0507, Reno, NV, Jan. 1990.

[2]Shirayama, S., "Computational Study of Flow Separation in Three-Dimensions," Ph.D. Dissertation, Univ. of Tokyo, Tokyo, Japan, 1987 (in Japanese).

[3]Shirayama, S., and Kuwahara, K., "Flow Visualization in Computational Fluid Dynamics," *International Journal of Supercomputer Applications*, Vol. 4, No. 4, 1990, pp. 66–80.

[4]Takami, H., and Kuwahara, K., "Numerical Study of Three-Dimensional Flow Within a Cubic Cavity," *Journal of Physical Society of Japan*, Vol. 37, No. 6, 1974, pp. 1695–1698.

[5]Thompson, J. F., Warsi, Z. U. A., and Mastin, C. W., *Numerical Grid Generation*, North-Holland, New York, 1985, pp. 95–135.

[6]Kawamura, T., Kuwahara, K., and Takami, H., "Computation of High Reynolds Number Flow Around a Circular Cylinder with Surface Roughness," *Fluid Dynamics Research*, Vol. 1, 1986, pp. 145–162.

[7]Shirayama, S., "A Structure of Leading-Edge and Tip Vortices at a Delta Wing," AIAA Paper 89-1803, Buffalo, NY, June 1989.

[8]Jenson, V. G., "Viscous Flow Round a Sphere at Low Reynolds Numbers," *Proceedings of the Royal Society of London*, Vol. 249, A, 1959, pp. 346–366.

[9]Rimon, Y., and Cheng, S. I., "Numerical Solution of a Uniform Flow over a Sphere at Intermediate Reynolds Numbers," *Physics of Fluids*, Vol. 12, No. 5, 1969, pp. 949–959.

[10]Le Clair, B. P., and Hanielec, A. E., and Pruppachr, H. R., "A Numerical Study of the Drag on a Sphere at Low and Intermediate Reynolds Numbers," *Journal of the Atmospheric Sciences*, Vol. 27, 1970, pp. 308–315.

[11]Dennis, S. C. R., and Walker, J. D. A., "Calculation of the Steady Flow Past a Sphere at Low and Moderate Reynolds Numbers," *Journal of Fluid Mechanics*, Vol. 48, Part 4, 1971, pp. 771–789.

[12]Nakabayashi, K., and Aoi, T., "Comparison of the Analytical Solutions with Numerical Solutions for Viscous Flows Past a Sphere," *Nagare*, Vol. 8, 1989, pp. 48–55 (in Japanese).

[13]Taneda, S., "Experimental Investigaion of the Wake Behind a Sphere at Low Reynolds Numbers," *Journal of the Physical Society of Japan*, Vol. 11, No. 10, 1956, pp. 1104–1108.

[14]Pruppachr, H. R., Le Clair, B. P., and Hanielec, A. E., "Some Relations Between Drag and Flow Pattern of Viscous Flow Past a Sphere and a Cylinder at Low and Intermediate Reynolds Numbers," *Journal of Fluid Mechanics*, Vol. 44, Part 4, 1970, pp. 781–790.

[15]Anderson, C. R., Greengard, C., Greengard, L., and Rokhlin, V., "On the Accurate Calculation of Vortex Shedding," *Physics of Fluids A*, Vol. 2, No. 6, 1990, pp. 883–885.

[16]Achenbach, E., "Vortex Shedding from Spheres," *Journal of Fluid Mechanics*, Vol. 62, Part 2, 1974, pp. 209–221.

[17]Taneda, S., "Visual Observations of the Flow Past a Sphere at Reynolds Numbers Between 10000 and 100000," *Journal of Fluid Mechanics*, Vol. 85, Part 1, 1978, pp. 187–192.

[18]Pao, H. P., and Kao, T., "Vortex Structure in the Wake of a Sphere," *Physics of Fluids*, Vol. 20, No. 2, 1977, pp. 187–191.

[19]Asaka, S., and Oshima, Y., "Shedding Vortices from Spheres," *Natural Science Report of the Ochanomizu University*, Vol. 28, No. 1, 1977, pp. 35–42.

[20]Kim, I., and Pearlstein, A. J., "Stability of the Flow Past a Sphere," *Journal of Fluid Mechanics*, Vol. 211, 1990, pp. 73–93.

[21]Schlichting, H., *Boundary-Layer Theory*, 7th ed., McGraw-Hill, New York, 1979, p. 17.

[22]Tobak, M., and Peak, D. J., "Topology of Three-Dimensional Separated Flows," *Annual Review of Fluid Mechanics*, Vol. 14, 1982, pp. 61–85.

[23]Murman, E. M., and Powell, K. G., "Trajectory Integration in Vortical Flows," *AIAA Journal*, Vol. 27, No. 7, 1988, pp. 982–984.

[24]Smith, M. H., Van Dalsen, W. R., Dougherty, F. C., and Buning, P. G., "Analysis and Visualization of Complex Unsteady Three-Dimensional Flows," AIAA Paper 89-0139, Reno, NV, Jan. 1989.

[25]Perry, A. E., and Chong, M. S., "A Description of Eddying Motions and Flow Patterns using Critical-Point Concepts," *Annual Review of Fluid Mechanics*, Vol. 19, 1987, pp. 125–155.

[26]Dallmann, U., "Three-Dimensional Vortex Structures and Vorticity Topology," *Fluid Dynamics Research*, Vol. 3, 1988, pp. 183–189.